A fluid-structure interaction solver for the fluid flow through reed type valves

IOP Conf. Series: Materials Science and Engineering **232** (2017) 012032 doi:10.1088/1757-899X/232/1/012032

A fluid-structure interaction solver for the fluid flow through reed type valves

I González, A Naseri, J Rigola, C D Pérez-Segarra and A Oliva

Heat and Mass Transfer Technological Center (CTTC), Universitat Politècnica de Catalunya - BarcelonaTech (UPC), ESEIAAT, Colom 11, 08222, Terrassa (Barcelona), Spain

E-mail: nacho@cttc.upc.edu

Abstract. Suction and discharge processes with self actuated valves have a major influence in efficiency and reliability of hermetic reciprocating compressors. Understanding the operation completely in order to enhance compressor's design needs precise prediction of the fluid-structure interaction complexities involved in these processes. This paper presents a comprehensive description of a numerical methodology to account for the coupled behaviour of a reed valve and a turbulent flow. The method is based on a partitioned semi-implicit scheme that only strongly couples the fluid pressure term to the structural solver. A three-dimensional CFD analysis with LES turbulence modelling is used for the flow while a combination of plate theory and mode summation method is used for the solid. The dynamically changing domains are tackled by means of lagrangian and arbitrary lagrangian-eulerian approaches for the solid and the fluid, respectively. The whole model is compared with experimental data at Reynolds number 10,000, showing good agreement in lift amplitude and deformation fluctuations. Finally, as an illustrative case, results regarding lift, pressures, force and effective areas are compared with those of a valve with wider gland.

1. Introduction

Design of reed valves is a challenging task and is of great relevance for the overall performance of hermetic reciprocating compressors [1, 2]. They are involved in suction and discharge processes, which are responsible for nearly half of the total thermodynamic losses of the compressor [3]. But besides efficiency, reliability is also influenced, since the repetitive loading of the valves is the most common cause of failure of the machine [4, 5].

The problem presents different complexities such as high pressure and velocity gradients, flow detachment, turbulence, collisions and fluid-structure multi-physics coupling. Traditionally the process has been tackled by means of one-dimensional lumped models [6], which have been proved to work reasonably well for broad design studies. However, a more detailed approach needs to be considered in order to fully understand the flow topology and optimise valve design. In the last years, following an enhance in computational resources, a growing research on 3D computational fluid dynamics (CFD) simulations for valve flow has been carried out. A verified fluid-structure interaction (FSI) model, which strongly couples both 3D CFD and finite element structural solvers, was thoroughly explained and used for reed valves in [7]. Besides, different CFD analysis considering FSI have been performed which include comparison with experimental data. Some examples can be found in [8, 9, 10, 11]. They mostly focused on the valve response

rather than on the description of the numerical methodology or the results regarding the flow behaviour.

The objective of this work is to provide an insight into a numerical methodology which is able to perform a complete three-dimensional analysis of the turbulent valve flow. The method is based on a new strong fluid-structure coupling algorithm which ensures numerical stability with a moderate increase in computational cost. First, an experimental test is numerically replicated. Then the case is simulated with a variation in the original design of the valve to evaluate the sensitivity of the system and to prove the potential of the numerical procedure to optimise valve designs.

2. Numerical methodology

A partitioned approach is followed to solve the FSI problem, which uses independent solvers for fluid and structural sub-problems and adopts a coupling scheme to account for their interaction. The elastic reed motion is modelled using the normal mode summation method, within a Lagrangian mesh, thus taking the local loads and bending deformations into account with negligible computational effort. On the other hand, the fluid flow is solved with a parallel CFD code on a 3D unstructured grid, which will deform according to the dynamic domain defined by the solid position. Throughout valve opening, a gap will appear between the valve and the seat, making necessary a new set of fluid elements in that zone. In order to avoid a remeshing procedure, there will be moving elements which first perform as solid, i.e. the valve seat, and later as fluid, i.e. the gap in between. This change in the nature of the elements is achieved using an immersed boundary method (IBM) [12].

Next, the governing equations of both sub-domains as well as the moving mesh technique and the coupling algorithm are described.

2.1. Governing equations

The flow is governed by the incompressible Navier-Stokes and continuity equations, formulated within an arbitrary lagrangian-eulerian moving domain framework,

$$\frac{\partial \vec{u}}{\partial t} + (\vec{u} - \vec{u}_w) \cdot \nabla \vec{u} = -\frac{1}{\rho_f} \nabla p + \frac{\mu}{\rho_f} \Delta \vec{u} \tag{1}$$

$$\nabla \cdot \vec{u} = 0 \tag{2}$$

where p and $\vec{u}$ are the fluid pressure and velocity, respectively. A fractional step projection method is adopted to decouple the unknowns and solve equations 1 and 2 [13]. Considering an explicit time advancement, the projection method yields to a three step solution procedure which can be written as:

$$\vec{u}^p = \vec{u}^n - \Delta t \left[(\vec{u}^n - \vec{u}_w) \cdot \nabla \vec{u}^n - \frac{\mu}{\rho_f} \Delta \vec{u}^n \right] \tag{3}$$

$$\Delta p^{n+1} = \frac{\rho_f}{\Delta t} \nabla \cdot \vec{u}^p \tag{4}$$

$$\vec{u}^{n+1} = \vec{u}^p - \frac{\Delta t}{\rho_f} \nabla p^{n+1} \tag{5}$$

with $\vec{u}^p$ denoting the predicted velocity. Fully conservative symmetry-preserving schemes [14] are used for the spatial discretization, whereas the wall-adapting local-eddy viscosity model (WALE) is used to describe the turbulent flow.

In regards to the reed structure, the momentum equation for an isotropic plate on (x, y) under transverse loading, having considered the assumptions of Kirchhoff-Love theory, is:

$$D \nabla^4 d_z(x, y, t) + 2 \rho_s h \ddot{d_z}(x, y, t) = \sigma_{\Gamma, z}(x, y, t) \tag{6}$$

where D is the bending stiffness, d_z the normal displacement, h the uniform thickness and $\sigma_{\Gamma,z}$ the normal component of the traction exerted on the plate surface Γ. According to the mode superposition method [15, 16], the motion of a vibrating system can be approximated by the sum of a limited number of normal modes m, weighted by generalised coordinates q_m:

$$d_z\left(x,y,t\right) \approx \sum_{m=1}^{N} q_m(t)\phi_m(x,y) \tag{7}$$

where $\phi_m(x,y)$ are the deformation patterns of the vibration modes, in z direction.

The combination of equations 6 and 7 leads to one generalised momentum equation for each mode [2],

$$\ddot{q}_m(t) + \omega_m^2 q_m(t) = \frac{\int_\Gamma \phi_m(x,y)\sigma_{\Gamma,z}(x,y,t)d\Gamma}{\rho_s h \int_\Gamma \phi_m^2(x,y)d\Gamma} \tag{8}$$

where ω_m are the natural radial frequencies, which can be found, along with the mode shapes, previously to the simulation with a normal mode analysis. Therefore, once the loads on the structure are known, the generalised coordinates q_m can be calculated with a numerical time integration scheme, in this case with the Newmark one.

Finally, the impact between valve and seat is estimated as a change in its velocity regulated by a coefficient of restitution C_r. As soon as contact is detected, the generalised velocities are corrected as

$$\dot{q}_m(t^{n+1}) = -C_r \dot{q}_m(t^n) \tag{9}$$

When C_r is set to one, all the kinetic energy is preserved after impact. Whilst this simple approach avoids body overlapping and controls the energy dissipation, it can be inaccurate from a continuum medium perspective, since it does not take into account the effect of local consecutive impact events.

2.2. Moving mesh technique

The fluid mesh adaptation is governed by the equations of linear elasticity, similarly to [17] but with a finite-volume discretization. By introducing a volume-based stiffening directly in the Young modulus of the elements

$$E_i = V_i^{-\chi}, \quad \chi \geq 0 \tag{10}$$

the major distortion will be absorbed by the larger elements, hence maintaining a good quality in the smaller elements which are located near the solid boundaries.

The velocity of the frame of reference $\vec{u}_w$ is here evaluated in the control volume faces. To calculate these velocities, the volume swept by a face between two time steps can be exactly computed while respecting the conditions imposed by the geometric conservation law [18], which yields:

$$\frac{d}{dt}\int_\Omega dV + \oint_{\partial\Omega} \vec{u}_w \cdot \vec{n} dS = 0 \tag{11}$$

2.3. Fluid-structure coupling scheme

On the fluid-structure interface Γ, there is a Dirichlet boundary condition for the fluid and a traction (Neumann condition) for the structure. The former as a function of the structure displacement $\vec{u}_\Gamma = \partial\vec{d}/\partial t$, and the latter as a function of fluid velocity and pressure $\vec{\sigma}_\Gamma\left(\vec{u},p\right)$.

Having updated the boundary velocity $\vec{u}_\Gamma$ with $\vec{d}$, the fluid solver is able to find p and $\vec{u}$ in the fluid domain and, in this manner, evaluate the traction distribution on the solid surface: $\vec{\sigma}_\Gamma = \vec{F}(\vec{d})$. Likewise, the structural solver will find the appropriate $\vec{d}$ derived from the fluid

load: $\vec{d} = \vec{S}(\vec{\sigma}_\Gamma)$. Therefore, the coupled fluid-structure system of equations reduces into an interface problem of the form:

$$\vec{S} \circ \vec{F}(\vec{d}) - \vec{d} = 0 \tag{12}$$

In most of the previous works, the coupling is treated explicitly for simulating suction/discharge processes, which means solving each domain by employing the other-domain data from the previous time step. Nevertheless, it has been shown that explicit schemes may cause numerical instability when both physics are strongly coupled [19]. In order to overcome this issue, a novel semi-implicit coupling scheme has been developed [20]. The new approach leverages the projection method to implicitly couple only the fluid pressure term to the structure, instead of the whole fluid set of equations. By doing so, the algorithm ensure an accurate and stable resolution of the coupled problem avoiding excessive computational cost.

Therefore, at the beginning of the time step the fluid mesh is adapted in accordance with the last deformation found for the solid, and the velocities of the faces $\vec{u}_w$ are evaluated. With these updates, the first step of the projection method (Equations 3) can be used to find the fluid predicted velocities $\vec{u}^p$. Then, the strong FSI coupling starts by iteratively solving Equations 4 and 8. As soon as the convergence criterion is met, the fluid velocity correction (Equation 5) is evaluated to finally finish the time step simulation.

To solve the nonlinear FSI iterative system, a fixed-point solver with a block Gauss-Seidel method and Aitken's dynamic relaxation has been chosen for this study. Aitken's dynamic relaxation mitigates possible convergence problems of the Gauss-Seidel method and reduces the number of required iterations.

3. Definition of the case

Aiming at validating the numerical methodology, here a comparative study of the experimental case carried out in [21] is presented. It was focused on the valve motion under the load of a developed and stationary air flux. The set-up consists of a feeding tube with $d = 34.9$ mm in diameter, a plate where the reed valve lies and an empty space downstream. In Figure 1 there are the dimensions of the valve as well as those of the cylindrical domain chosen for the simulations. The valve diameter D is 1.3 times the orifice diameter d. Apart from the original valve geometry, a modified version with a wider gland has been considered so as to highlight the differences regarding the coupled system performance. The former will be called valve A whereas the latter valve B.

The temperature of the air is 25 $^{\circ}$C and ambient pressure is defined at the outlet. The physical properties of the flexible valve are set to be: $\rho_s = 7850$ kg/m^3, $\nu = 0.3$ and $E = 2 \cdot 10^{11}$ Pa. An average coefficient of restitution of $C_r = 0.3$ has been fixed for the seat impact dissipation according to [22]. The inlet velocity of the fluid is determined so that the Reynolds number is $10,000$:

$$Re = \frac{\rho_f \bar{u}_z d}{\mu} \tag{13}$$

where $\bar{u}_z$ is the axial bulk velocity. The inlet boundary condition is implemented as a developed turbulent pipe flow. The averaged velocity profile has been extracted from [23] and is depicted in Figure 2. In addition, synthetic inflow conditions are prescribed at the boundary like in [24] to reproduce the transient turbulent nature of the flow (Figure 3). To do so, the turbulent statistics for wall flow at $Re = 11,700$ found in [25] have been used.

The results presented in this section have been obtained with a computational mesh of around $3 \cdot 10^5$ control volumes. This discretization has been proved to provide a suitable converged solution for the present flow configuration.

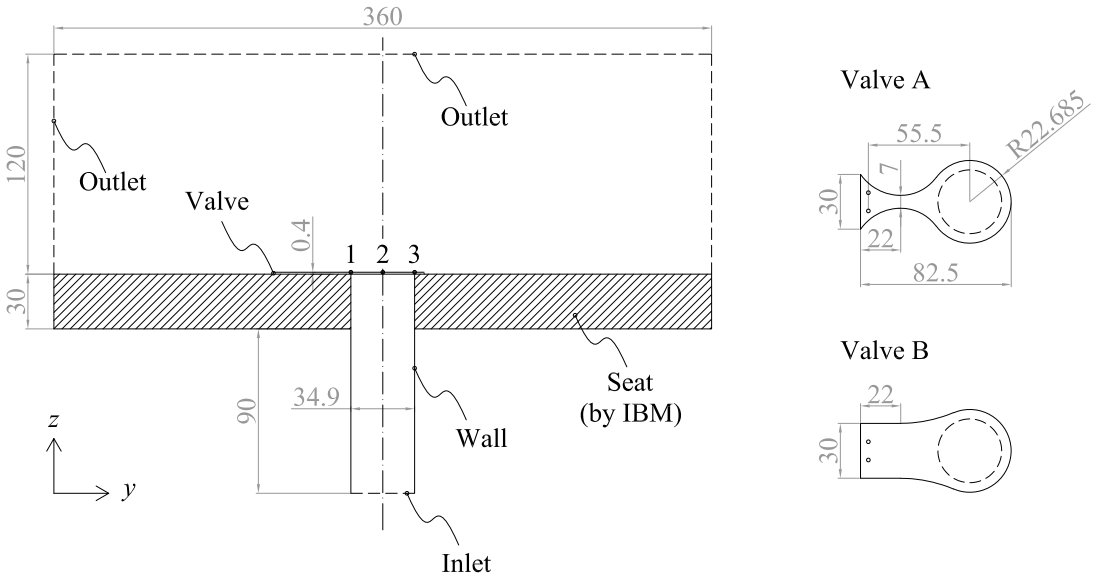

Figure 1: Section of the computational domain and geometry of the valves (dimensions in mm). Points 1, 2 and 3 for lift measurements.

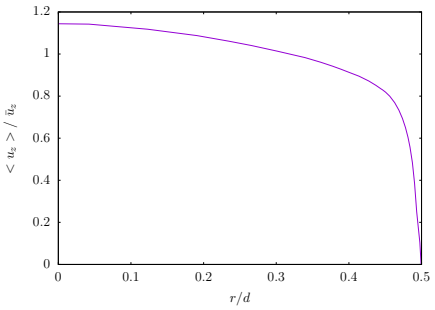

Figure 2: Averaged inlet velocity profile.

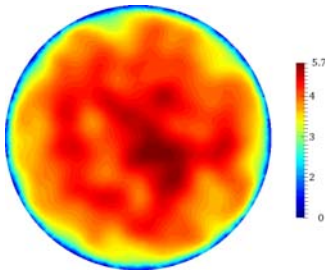

Figure 3: Instantaneous inlet velocity map in [m/s].

4. Numerical results

First, a linear modal analysis has been carried out for the reeds with a clamped boundary condition in their root. The results, obtained with a commercial structural software, are shown in Figure 4. Only the first four modes have been taken into account for this study. As can be seen, the first natural frequency of the design A is very close to the value determined in [21], 31.4 Hz. The geometry B evidently has larger mass and stiffness as a result of the gland widening. Observing the frequencies, the major rise is in the stiffness, since all but the fourth mode vibrate at higher rates than the original valve.

Under the fluid load, the valve bends and starts fluttering with impacts on the seat. The system rapidly reaches a periodic steady state of operation with constant amplitude in lift (h) and pressures (p). This cyclic response is shown in Figure 5, where the displacement of point 1 (see Figure 1) of valve A is plotted along with the experimental measurements. Although the resultant prominent frequency is pretty similar (f_A is 58.6 Hz numerically while it was 57.9 Hz experimentally) there is a considerable deviation in the oscillation peak. The model over-predicts the maximum aperture by approximately 16 %. However, the amplitude error falls down to 6 % and the perturbations within a smooth sinusoidal motion agree with the experiment.

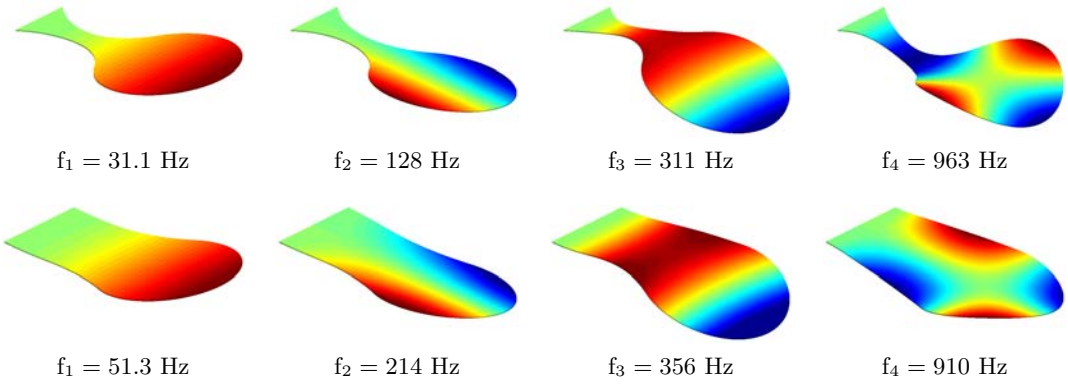

Figure 4: Normal modes of vibration of valves A (top) and B (bottom).

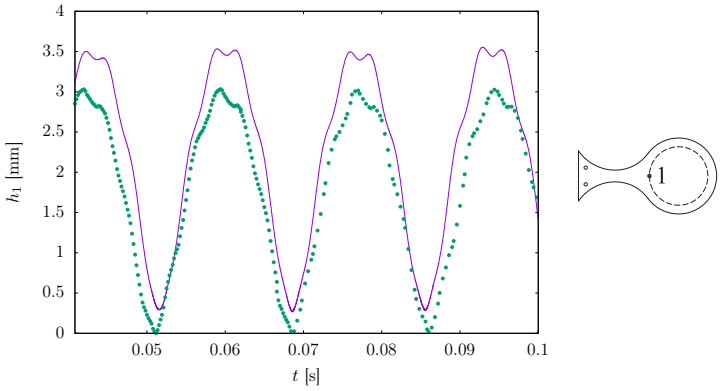

Figure 5: Valve lift with design A in point 1. Numerical results (——) and measures from Dr. José Luis Gasche (●).

Observing the displacements of the three valve control points (Figure 6 (a)), one may point out the impact evaluation as the most plausible cause of the mentioned discrepancies. The graph shows there is not a flat contact with the seat, because each of the three points would reach the seat at a different time. This is due to the effect of higher vibration modes on the valve transient deformation. With the approximation used for the impact (Equation 9), not all valve points are colliding with the seat and the valve eventually rises earlier than expected. Thus, it would be worth implementing a more accurate model for this critical event. On the other hand, the configuration B does not exhibit such an issue regarding the collision. Even though there is also an influence of other modes of vibration apart from the first –noticeable in the fluctuation of points 1 and 3 of Figure 6 (b)– all three points hit the seat at the same time, giving rise to an almost flat contact.

The greater stiffness of option B is responsible for the decrease in lift amplitude (~ 1.4 times lower) and the increase in flutter frequency ($f_B = 90.7$ Hz). The momentum carried by the flow is unable to open valve B as much as valve A, and a greater force is required in order to bend the former by the same angle as the latter. This fact can be distinctly observed by comparing the flow pressure exerted on the valve for a common valve height. In Figure 7 this pressure is depicted at instant t_1, when both valves share the same displacement measured in the port axis (see Figure 6). As expected, the pressure is considerably higher in case B. Besides, the pressure

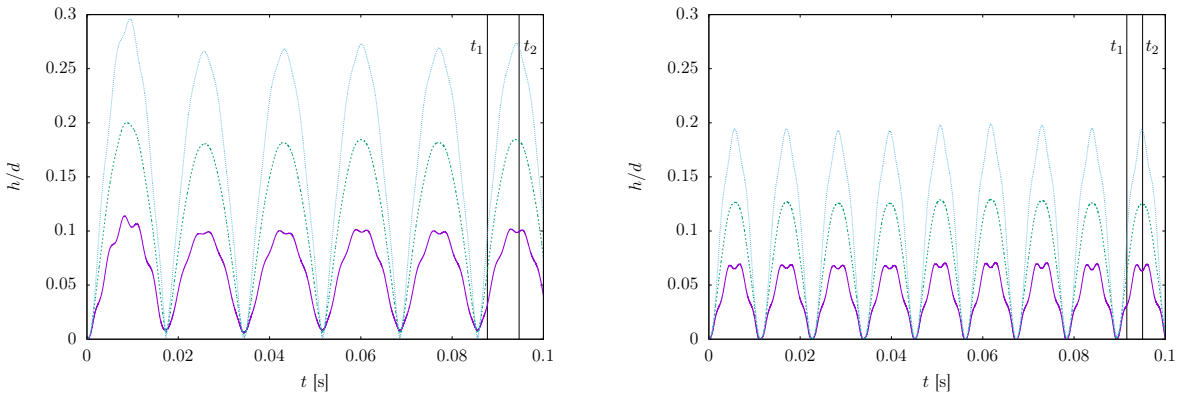

(a) Valve A (b) Valve B

Figure 6: Valve lift in points 1 (——), 2 (- - - -) and 3 (·····).

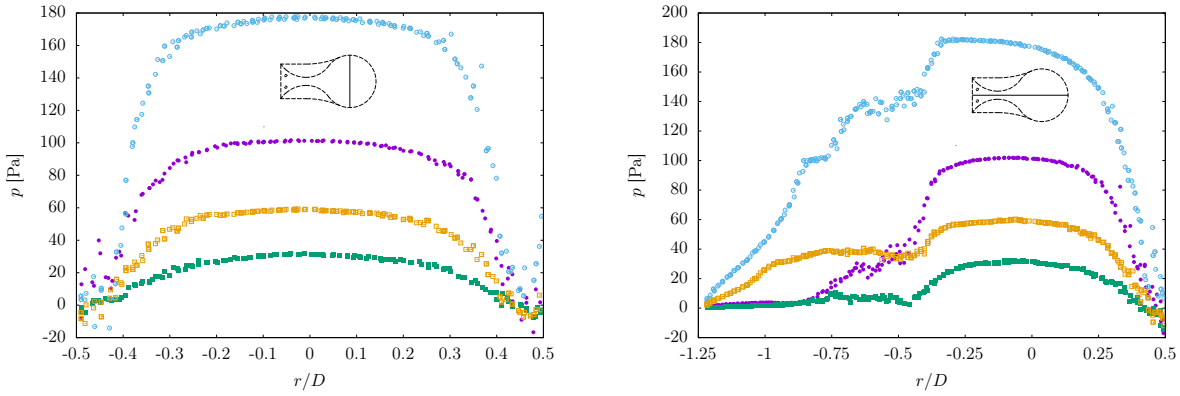

Figure 7: Pressure over the lower face of the valve at time t_1 (● A and ○ B) and t_2 (■ A and □ B).

along the longitudinal line shows that this variable is not symmetric with respect to the channel axis, as a result of the valve geometry and its deformed shape.

The same profiles at instant t_2 are presented in Figure 7 as well, which corresponds to the time when the maximum valve lift is achieved by each geometry. They show the clear effect of height and flow area on the fluid pressure. Having a higher valve lift, valve A allows the flow to change its direction sooner and reduce the axial momentum carried when it impinges into the valve. In addition, the fluid velocity crossing the larger gap between valve and valve seat should not accelerate as much as with valve B, as can be seen in the velocity field of Figure 9. It can also be identified the separation bubble which is generated at the outside edge of the valve seat.

In order to check the influence of the wider gland on the outflow area, the effective flow area defined for incompressible flow as:

$$(KA)_e = \frac{\dot{m}}{\sqrt{2\rho_f(p_{inlet} - p_{outlet})}} \tag{14}$$

is depicted in Figure 10 (a) as a function of valve height. The value has been averaged taking into account all the periodic oscillations simulated. Due to the incompressibility assumption, the effective flow area is only geometry dependent and a proportional relation is found with

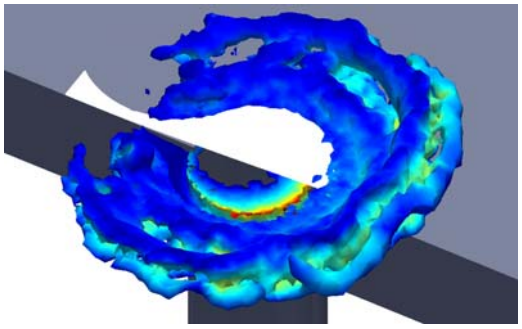

(a) Valve A

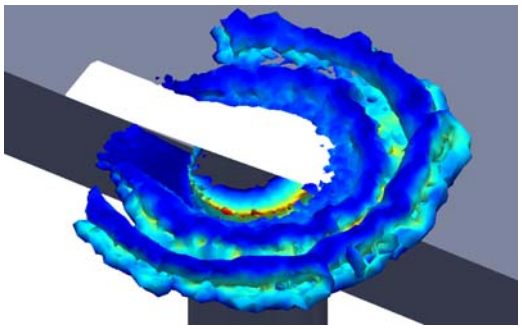

(b) Valve B

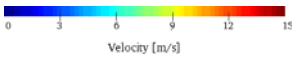

Figure 8: Contour surface for 1000 rad/s of vorticity at t_1.

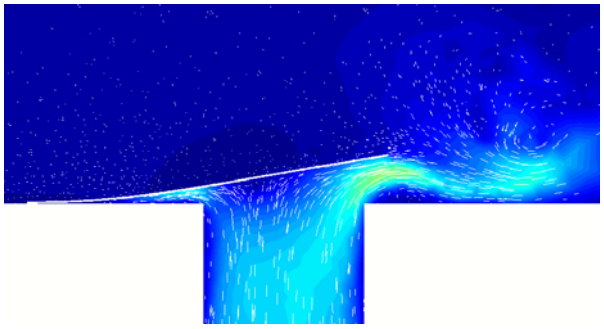

(a) Valve A

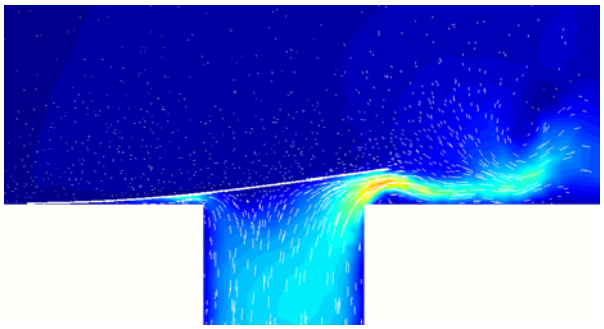

(b) Valve B

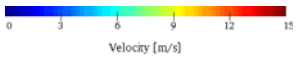

Figure 9: Velocity magnitude map and velocity vectors at t_2.

the valve lift. As can be observed, the wider body of valve B does not generate a significant difference in the effective flow area compared with A. Since the mass flow $\dot{m}$ does not vary, this implies that both valves produce almost the same pressure drop for a given displacement. In fact, the air flow pattern is pretty similar in A and B at the highlighted time instant t_1, when both are equally opened, as can be seen in the vorticity maps of Figure 8.

In the same manner, in Figure 10 (b) the averaged effective force area is presented. It has been calculated as the fraction between thrust force F and pressure drop:

$$A_F = \frac{F}{p_{inlet} - p_{outlet}} \tag{15}$$

The graph shows how the pressure rises to a different extent as the fluid reaches each valve, because of their different stiffness. In both cases the effective force area decreases with increasing valve height. This is explained by the flow detachment and the separation bubble developed between valve and seat, which create a negative pressure that counteracts the positive pressure over the port and diminishes the net force. A similar drop in the effective force area has been previously detected for small displacements of the valve and strong Bernoulli effect in [26, 27, 28] for example.

It has been stated above that valves A and B cause the same instantaneous pressure drop with a common valve height. However, this does not imply that the process efficiency is equivalent for both valves, since they have different oscillation rates and lift peaks. In this case, one can analyse the total pressure drop per time unit in order to compare the difficulty the air must

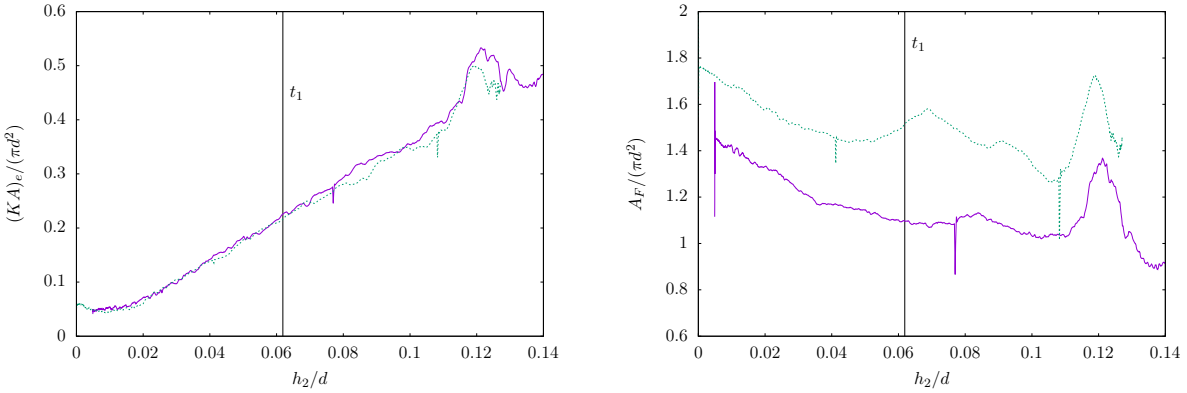

(a) Effective flow area. (b) Effective force area.

Figure 10: Cycle-averaged parameters of case A (——) and B (- - - -) as a function of displacement of point 2 during the opening process.

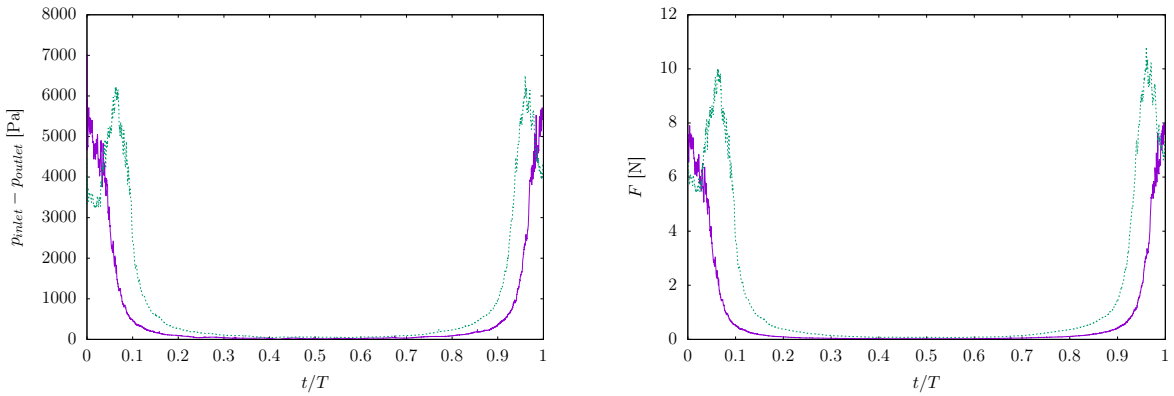

(a) Pressure drop. (b) Net force on the valve.

Figure 11: Cycle-averaged variables of case A (——) and B (- - - -) as a function of dimensionless time.

withstand to flow out the channel. Pressure drop per oscillation period is presented in Figure 11 (a). The integral of this graph indicates that 573 and 1020 Pa per cycle are needed in cases A and B, respectively. If this value is multiplied by the cycle frequency, then the total pressure drop can be obtained: 33,600 Pa/s with valve A whereas 92,000 Pa/s with valve B. Therefore, the outflow efficiency of this steady flow is far better with valve A, basically due to its higher flexibility.

Finally, in Figure 11 (b) the thrust force on the valve plate is presented. It shows the rise in the fluid force as soon as the valve closes, i.e. as soon as the outflow area diminishes and the valve surface and jet velocity become more perpendicular.

5. Conclusions

An in-house numerical methodology to solve the fluid-structure interaction of the turbulent flow through self actuated reed valves has been presented. The platform strongly couples a three-dimensional CFD solver with turbulence modeling to a structural model for vibrating plates. A moving mesh technique along with the arbitrary lagrangian-eulerian formulation deforms the

fluid domain according to the valve deformation. In order to avoid remeshing, the immersed boundary method defines the position of the valve seat. Validation of the model is carried out by comparing the fluttering of a suction valve under a stationary flow at Reynolds number 10,000. The results show that the method is able to yield a representative description of the flow field surrounding the valve. However, a more detailed analysis of the impact between reed and other bodies is necessary to resolve the discrepancies detected in the valve lift. The same set-up is used to test a similar valve with a wider gland body in order to showcase the potentiality of the proposed methodology to optimise valve designs. Although lower stresses are expected with this modification, its higher stiffness reduces the maximum effective flow area and increases the pressure drop, hence worsens the process efficiency.

Acknowledgments

We would like to thank Dr. José Luis Gasche and his team at Universidade Estadual Paulista for providing the experimental measures and for their valuable comments. This work has been financially supported by the Ministerio de Educación, Cultura y Deporte, Spain (FPU13 fellowships).

References

[1] Soedel W 1984 *Design and Mechanics of Compressor Valves* (Purdue University)
[2] Soedel W 1992 *Mechanics, Simulation and Design of Compressor Valves, Gas Passages and Pulsation Mufflers* (Purdue University)
[3] Ribas F A, Deschamps C J, Fagotti F, Morriesen A and Dutra T 2008 *Int. Compressor Engineering Conf.* (Indiana)
[4] Leonard S M 1996 *Hydrocarb. Process.* **75** 67 – 74
[5] Woo S, O'Neal D L and Pecht M 2010 *Eng. Fail. Anal.* **17** 979 – 991
[6] Boeswirth L 1996 *Int. Compressor Engineering Conf.* (Indiana)
[7] Schildhauer M and Spille-Kohoff A 2014 *Prog. in Comp. Fluid Dy.* **14** 38–48
[8] Mayer J, Bjerre P and Brune F 2014 *Int. Compressor Engineering Conf.* (Indiana)
[9] Lemke N C, König M, Hennig J, Försterling S and Köhler J 2016 *Int. Compressor Engineering Conf.* (Indiana)
[10] Parihar A, Myszka D, Robinet B and Hodapp T 2016 *Int. Compressor Engineering Conf.* (Indiana)
[11] Gasche J L, de Lima Dias A D S, Bueno D D and Lacerda J F 2016 *Int. Compressor Engineering Conf.* (Indiana)
[12] Favre F, Antepara O, Lehmkuhl O, Borrell R and Oliva A 2014 *Joint WCCM - ECCM - ECFD 2014 Congress* (Barcelona)
[13] Jofre L, Lehmkuhl O, Ventosa J, Trias F X and Oliva A 2014 *Numer. Heat Transf. Part B Fundam.* **65** 53–79
[14] Trias F, Lehmkuhl O, Oliva A, Pérez-Segarra C and Verstappen R 2014 *J. Comput. Phys.* **258** 246 – 267
[15] Thomson W 1998 *Theory of Vibration with Applications (5th Edition)* (Taylor & Francis)
[16] Bathe K J 1996 *Finite Element Procedures* (Prentice Hall)
[17] Smith R 2011 A pde-based mesh update method for moving and deforming high reynolds number meshes *49th AIAA Aerospace Sciences Meeting* (Orlando)
[18] Lesoinne M and Farhat C 1996 *Comput. Methods in Appl. Mech. Eng.* **134** 71 – 90
[19] Causin P, Gerbeau J F and Nobile F 2005 *Comput. Methods in Appl. Mech. Eng.* **194** 4506 – 4527
[20] Naseri A, Lehmkuhl O, Gonzalez I and Oliva A 2016 *J. Phys.: Conf. Series* **745** 032020
[21] Gasche J L, Arantes D M and Andreotti T 2014 *Int. Compressor Engineering Conf.* (Indiana)
[22] Habing R A and Peters M C A M 2006 *Journal of Fluids and Structures* **22** 683 – 697
[23] Kim J, Moin P and Moser R 1987 *J. Fluid Mech.* **177** 133 – 166
[24] Rigola J, Aljure D, Lehmkuhl O, Pérez-Segarra C D and Oliva A 2015 *IOP Conf. Ser.: Mater. Sci. Eng.* **90** 012026
[25] El Khoury G K, Schlatter P, Noorani A, Fischer P F, Brethouwer G and Johansson A V 2013 *Flow Turbul. Combust.* **91** 475 – 495
[26] Schwerzler D D and Hamilton J F 1972 *Int. Compressor Engineering Conf.* (Indiana)
[27] Ferreira T S and Lainor J 1986 *Int. Compressor Engineering Conf.* (Indiana)
[28] Deschamps C J, Ferreira R T S and Prata A T 1988 *Int. Compressor Engineering Conf.* (Indiana)